Experimental and CFD analysis of a floating offshore wind turbine under imposed motions

Journal of Physics: Conference Series **2767** (2024) 062010 doi:10.1088/1742-6596/2767/6/062010

Experimental and CFD analysis of a floating offshore wind turbine under imposed motions

Federico Taruffi[1], **Robin Combette**[2], **Axelle Viré**[1]

[1]Delft University of Technology, Faculty of Aerospace Engineering, Kluyerweg 1, 2629 HS Delft, the Netherlands

[2]Ecole Centrale de Nantes, LHEEA Lab., 1 rue de la Noë, 44321 Nantes Cedex 3, France

E-mail: F.Taruffi@tudelft.nl

Abstract.

The rotor of a floating offshore wind turbine experiences intricate aerodynamics due to significant motion in the floating foundation, necessitating a holistic understanding through a synergistic blend of experimental and numerical methodologies. This study investigates rotor loads and the emergence of unsteady phenomena for a floating offshore wind turbine under motion. The approach compares a wind tunnel experimental campaign on a moving scale model with large-eddy simulations. Importantly, both experimental and numerical setups were co-designed simultaneously to match conditions and allow a fair comparison. The experimental setup features a 1:148 scale model of the DTU 10MW reference wind turbine on a six degrees of freedom robotic platform, tested in a wind tunnel. Numerically, the LES code *YALES2*, employing an actuator line approach undergoing imposed motions, is used. Harmonic motions on one degree of freedom in surge and pitch directions are explored at various frequencies. Thrust force variation aligns with quasi-steady theory for both numerical and experimental results at low frequencies. However, higher frequencies reveal the rise of unsteady phenomena in experiments. Large-eddy simulations, coupled with an actuator line approach, provide additional insights into the near- and mid-wake response to imposed motions. This co-design approach between numerical and experimental tests enhances the comprehension of aerodynamic behaviour in floating offshore wind turbines, offering valuable insights for future designs.

1. Introduction

Floating offshore wind turbines (FOWTs) are widely considered promising technology but also come with new challenges. As a result of the floater motions, the rotor of a FOWT is subject to complex aerodynamics induced by large changes in the relative wind speed and potential interaction with the near-wake. A better understanding of the phenomena behind the aerodynamic behaviour of FOWTs demands a more holistic approach with a synergistic combination of experimental and numerical methodologies. Lab-scale experiments are highly relevant for directly capturing these phenomena and provide a means for the validation of numerical models that can be used as design tools.

Different model testing techniques have been developed, from more traditional physical scale models of the entire floating system tested in wave basins with the wind generated by fans, up to large-scale models tested in outdoor facilities and wind tunnel hybrid setups [1]. The latter can be preferred for aerodynamics-oriented studies as they combine a high-quality inflow

in a controlled environment with the possibility of actuating the model to mimic the floating motions.

Similarly, there is a wide variety of numerical models used to simulate the aerodynamic behaviour of rotors, which can be subjected to imposed motions or coupled with other models. They all have different levels of fidelity, but the complex, unsteady, and three-dimensional flows associated with FOWT make high-fidelity tools such as large-eddy simulations (LES) particularly relevant. Yet, blade-resolved LES remains extremely expensive, and the actuator line method (ALM) presents a good compromise between computational cost and required accuracy. This approach has been extensively used in fixed-bottom applications but also more recently for FOWT [2, 3]. It permits not only to accurately estimate the loads but also to capture the wake's development.

This work provides a combined numerical and experimental approach by conducting a wind tunnel experimental campaign on a moving wind turbine scale model and replicating the experiments with LES simulations. The aim is to evaluate the rotor loads of a floating offshore wind turbine subjected to motion and to investigate the rise of unsteady phenomena. Model scale experimental results are analysed in comparison with numerical results obtained with a LES model. The prediction capability of such numerical models is also an object of study. Finally, the numerical results also provide insight into the response of the near- and mid-wakes to these imposed motions.

2. Experimental setup

The experimental setup is composed of a wind turbine scale model placed on a hexapod capable of imposing motions in six degrees of freedom. The wind tunnel where the campaign took place is the Open Jet Facility of Delft University of Technology, a closed-loop facility with the contraction ending in a 2.85 $m \times 2.85$ m nozzle that opens in a 13 m wide and 8 m high open jet section. The tunnel ensures a uniform flow with a turbulence intensity of 0.5% at the testing location 1 m downstream of the nozzle outlet.

The wind turbine model is a $1:148$ scale of the DTU 10 MW reference wind turbine, featuring a fixed-pitch, 3-bladed rotor designed in [4]. The model uses the SD7032 airfoil, suitable for low-Reynolds applications. The rotor is scaled based on performance with the target of accurately reproducing the thrust curve of the full-scale turbine. Both the rotor, manufactured in carbon fiber as a single piece, and the cylindrical aluminium tower supporting the rotor-nacelle assembly present a stiff design to limit deflections. The rotor is driven by a servomotor and gearbox, hosted in the nacelle and connected to the rotor shaft. The main parameters of the wind turbine model are reported in Table 1.

The tower base is mounted on top of a parallel-kinematic robotic platform capable of six degrees of freedom motions. The commercially available Quanser Hexapod is used for its advantages in setup replication and portability. The hexapod underwent testing to assess its capabilities, resulting in the ability to operate loaded at frequencies up to 5 Hz without de-amplification.

A comprehensive measurement system includes a load cell for rotor forces and torques, accelerometers for vibrations and motion tracking, and sensors for wind turbine operating parameters. Data are recorded at a frequency of 1000 Hz. The setup is pictured and schematically represented in Figure 1 and 2, for more details on the experimental setup refer to [5].

2.1. Rotor thrust

To obtain the rotor loads when the turbine is set under motion, the force measurement needs to be corrected to subtract the inertial and gravitational contributions, isolating the aerodynamic contribution of interest induced by the dynamic motions. Each test with motion is repeated in

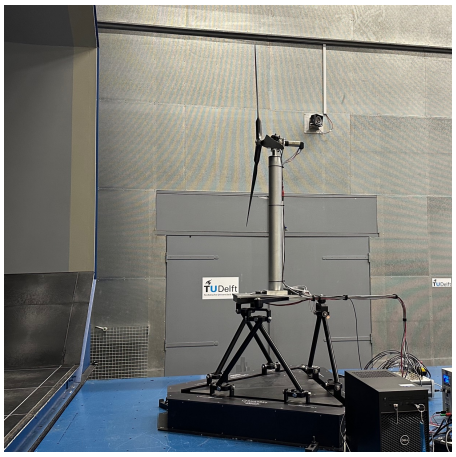

Figure 1: View of the experimental setup in the TU Delft wind tunnel facility.

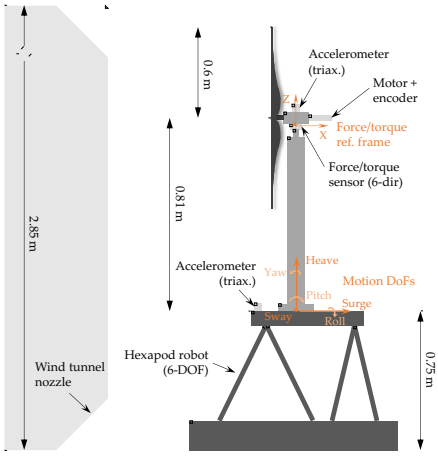

Figure 2: Setup scheme including sensors and reference systems.

Table 1: Main wind turbine model parameters.

Parameter	**Value**	**Unit**
Rotor diameter	1.2	m
Hub height	0.8	m
Nacelle mass	1.03	kg
Rotor mass	0.58	kg
Rated wind speed	4	m/s
Rated rotor speed	480	rpm

wind (wind blowing and rotor spinning) and no-wind (still air and rotor not spinning) conditions and the latter is used for the subtraction, which is performed in the frequency domain. The method to calculate the thrust force variation is the following:

$$|\Delta T| e^{i\phi\Delta T}\Big|_{\hat{f}} = |\Delta F_X^w| e^{i\left(\phi\Delta F_X^w - \phi a_{tb,X}^w\right)} - |\Delta F_X^{nw}| e^{i\left(\phi\Delta F_X^{nw} - \phi a_{tb,X}^{nw}\right)}\Big|_{\hat{f}}, \tag{1}$$

where $|\Delta T|$ is the thrust variation amplitude, $\phi\Delta T$ is the thrust variation phase, $|\Delta F_X^w|$ and $\phi\Delta F_X^w$ are the force variation amplitude and phase measured in $X-$direction (i.e. the direction of thrust) in wind condition, $|\Delta F_X^{nw}|$ and $\phi\Delta F_X^{nw}$ are the force variation amplitude and phase measured in $X-$direction in no-wind condition, $\phi a_{tb,X}^w$ and $\phi a_{tb,X}^{nw}$ are the phase of the acceleration measured in the same direction in wind and no-wind condition, used as reference, and $\hat{f}$ is the frequency of motion.

3. Numerical setup

This section outlines the numerical characteristics employed in conducting the simulations, covering the solver specifications, Actuator Line Method, and computational details.

3.1. The YALES2 solver

The large-eddy simulations are run using the Navier-Stokes solver *YALES2*, which uses a finite volume approach and whose main characteristics can be retrieved in [6]. In particular, the

equations in their incompressible formulation are solved using the *ICS* solver with 4th-order discretisation schemes for both the spatial and temporal terms (explicit method). More details on the resolution method are given in Benard et al. [7]. In addition, the SGS stress tensor is modeled using the dynamic Smagorinsky procedure as described by Germano et al. [8] and Lilly [9].

3.2. Actuator Line Method (ALM)

Due to the multi-scale nature of wind turbine flows, blade-resolved LES can lead to prohibitive computational time. Therefore, it is rather chosen to model the blades' effect on the flow field with a body force term $\vec{f}_{AL}$ computed via the Actuator Line Method (ALM). This approach, first introduced by Sørensen and Shen [10], represents the blades with discretised actuator lines and permits using coarser mesh near the rotor, hence significantly reducing the computational cost of LES. In brief, after discretising the blades in a certain number of actuator points N_{AL} in the spanwise direction, each blade section is considered under the blade element theory and the effective inflow velocity is evaluated. The direction and magnitude of this local velocity depend on the freestream and rotational velocities, the axial and azimuthal induction factors, accounting for the non-uniform distribution of the loads over the actuator disc, and the potential rotor motion. It permits the calculation of the effective angle of attack α which will be associated with lift and drag loads based on tabular airfoil data. After projection, the body force term is simply expressed as:

$$\vec{f}_{AL} = \frac{1}{2}\rho V_{eff}^2 c \left(C_l \vec{e}_L + C_d \vec{e}_D\right), \tag{2}$$

where C_l and C_d are respectively the lift and drag coefficients, c denotes the chord length, and V_{eff} is the local velocity in blade element theory.

Further details on the ALM implementation in *YALES2*, as well as its validation on a fixed-bottom wind turbine, are given in [7]. This implementation was later modified to account for motions in the six degrees of freedom and validated in [11].

3.3. Computational details

The computational domain is a simple rectangular cuboid with slip walls everywhere except at the outlet where a flat velocity profile is set to avoid back-flow issues, and at the inlet, where a uniform freestream velocity is prescribed. The wind tunnel effects caused by its particular geometry were evaluated using standard correction methods and found to be negligible. Therefore, the computational domain size is chosen in order to avoid any blockage effect. In a sensitivity analysis, four domains were compared with different cross-sectional areas and different length sizes ($L_x/D \times L_y/D \times L_z/D$ = 4×4×7 ; 6×6×10 ; 6×6×15 ; 8×8×15). Results suggest that $6D \times 6D$ for the cross-sectional area (resulting in a blockage ratio of 2.2%) and $10D$ in the streamwise direction, with the rotor being placed $3D$ downwind of the inlet, provide accurate results for a reasonable computational cost. The far-wake is not captured in the domain, but the focus is on the wind turbine loads, which are negligibly impacted by it, and on the near- and mid-wake development.

Following usual recommendations for ALM, the time step was set so that the blade tips do not cross more than one cell during one time step, leading to a Courant number of 0.65. This results in a time step around 6.10^{-4} s on average.

The unstructured mesh was constructed with four box-shaped refinement regions, decreasing progressively the cell size in the mid-wake, the near-wake, and finally near the rotor. The size of the cells in the most refined region near the rotor is directly related to the number of elements in which the blades are discretised (N_{AL}). Again, a sensitivity analysis on this number of elements was performed by comparing $N_{AL} = 32, 40, 46$ and $N_{AL} = 32$ was found sufficient to provide accurate results. The domain as well as the refinement regions are illustrated in Figure 3. The

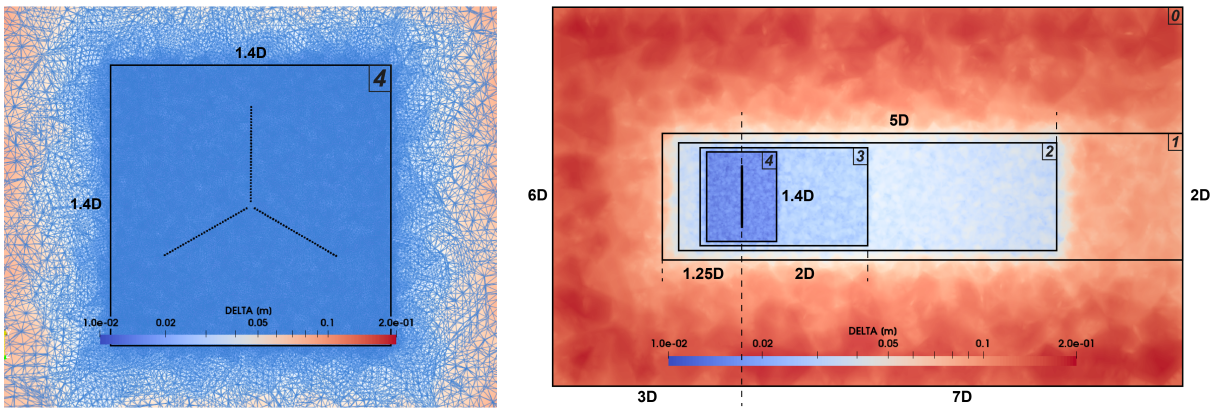

(a) Plane $z = 0$. (b) Plane $x = 0$.

Figure 3: Characteristic cell size Δ in the domain, the average size in the outer domain *(0)* is 0.125 m, 0.0625 m in the far-wake *(1)*, 0.025 m in the mid-wake *(2)*, 0.018 m in the near-wake *(3)*, 0.01 m near the rotor *(4)*.

final mesh used has about 32 million elements. Following common recommendations, the quality of the whole mesh was also verified by checking that at least 80% of the turbulent kinetic energy is resolved everywhere and at any time using Pope's criterion [12].

Finally, the simulations were run on the HPC12 cluster at TU Delft. As an example, the pitch case with $f = 1\ Hz$ ran for about 10h on 96 CPUs for a total time of simulations of $t_f = 6\ s$.

4. Test cases

The test cases selected for this work are sinusoidal motions on one degree of freedom in surge and pitch directions. The test matrix, displayed in Table 2, consists of a single hub-height velocity (ΔV dimensional, ΔV^* non-dimensional) for each degree of freedom and different frequencies (f), with the corresponding motion amplitude (A) calculated as $A = \Delta V / 2\pi f$. The turbine operates at the rated point, with a wind speed of 4 m/s and a constant rotor speed of 480 rpm corresponding to a tip-speed ratio of 7.5.

Table 2: Test cases chosen for the experimental vs. numerical comparison.

DOF	f $[Hz]$	ΔV^*	ΔV $[m/s]$	A
Surge	1	0.05	0.2	31.8 mm
Surge	2	0.05	0.2	15.9 mm
Surge	5	0.05	0.2	6.4 mm
Pitch	1	0.072	0.288	2.25 deg
Pitch	2	0.072	0.288	1.13 deg
Pitch	5	0.072	0.288	0.45 deg

5. Thrust variation

5.1. Surge

Here the results for the three surge cases described in Table 2 are given. The cases share the same normalised motion velocity ($\Delta V^* = 0.05$) and have different frequencies ($f = 1; 2; 5\ Hz$). The numerical thrust obtained is plotted in Figure 4, and compared with the experimental results in Table 3. In Figure 4, the static numerical results for the two extreme freestream velocities encountered during motion ($U_\infty = 4.0 \pm 0.2\ m/s$) are also given, they constitute the boundaries for the quasi-steady theory (QST). This theory calculates the thrust variation resulting from the dynamic change in relative wind speed caused by the motion considering the static thrust obtained at the extremes.

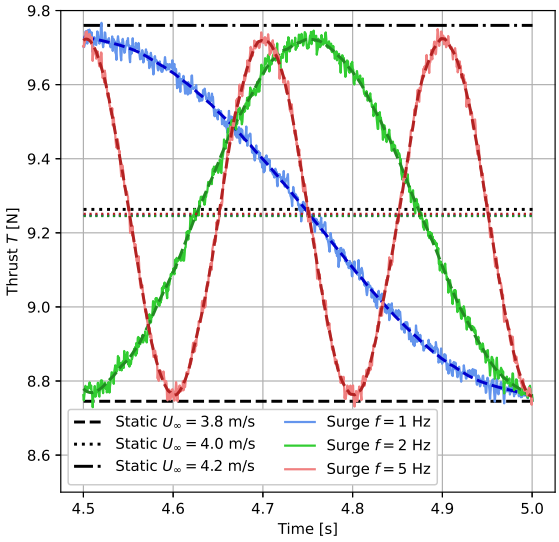

Figure 4: Numerical thrust force for surge motions with $\Delta V_p^* = 0.05$: non-filtered (coloured solid lines) and filtered (coloured dashed lines) solution, average over one motion period (coloured dotted lines) and static results (black lines).

Table 3: Comparison of rotor thrust for surge motion with $\Delta V^* = 0.05$, the first row stands for the QST prediction made from numerical static results.

Source	Frequency	$\overline{T}$ [N]	$\lvert\Delta T\rvert$ [N]	$\phi\Delta T$ [deg]
Static YALES2 + QST	$\forall\ f$	9.26	0.50	-90
YALES2	$f = 1$ Hz	9.24	0.48	-91.5
	$f = 2$ Hz	9.25	0.48	-91.2
	$f = 5$ Hz	9.25	0.48	-92.5
Exp.	$f = 1$ Hz	9.43	0.57	-89.1
	$f = 2$ Hz	9.39	0.59	-89.9
	$f = 5$ Hz	9.36	1.37	-91.6

The numerical results are well in accordance with the quasi-steady theory. For all frequencies, the phase difference is very close to the theoretical value, and the thrust variations match well the value expected from the static cases (at $U_\infty = 3.8\ m/s$ and $U_\infty = 4.2\ m/s$).

For the low frequencies ($f = 1; 2\ Hz$), the experimental results are in accordance with the QST as well. The thrust variation measured is slightly higher but this can be explained with the fact that the static numerical thrust was found to be slightly overestimated at lower velocities, hence reducing the amplitude of thrust variation expected from *YALES2*. On the other hand, a significant increase in thrust oscillation is measured experimentally at high frequency ($f = 5\ Hz$). This breakdown of quasi-steady theory for high frequencies is not observed in the numerical simulations and constitutes a substantial difference with the experimental results.

As a possible explanation for this discrepancy, the relatively low ratio between the amplitude of motion and the cell size near the rotor was advanced. Yet, the study of large-amplitude motions ($\Delta V^* = 0.75; 1$) and the use of a more refined mesh (cell size divided by 2.5 near the rotor) did not manage to capture unsteady effects numerically. It is believed that highly unsteady effects at the local airfoil scale may occur and cause such differences, as these cannot be captured with the ALM implementation.

On the mean thrust during surging, its value remains constant in the numerical results, with only a very slight increase in frequency, while the opposite trend is observed in the experiment.

5.2. Pitch

Similarly, the temporal evolution of the numerical trust is plotted for the three pitch cases in Figure 5. Two low-frequency cases ($f = 1, 2\ Hz$) and a high-frequency one ($f = 5\ Hz$) are considered. The results are compared with the experimental ones in Table 4.

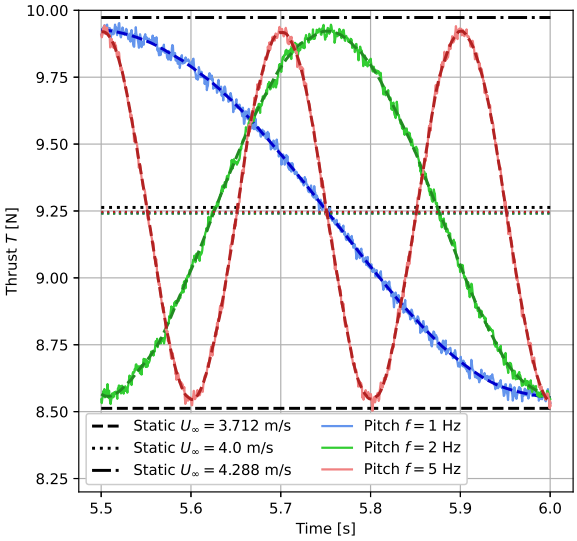

Figure 5: Numerical thrust force time history for pitch motions with $\Delta V_p^* = 0.072$: non-filtered (coloured solid lines) and filtered (coloured dashed lines) solution, average over one motion period (coloured dotted lines) and static results (black lines).

Most of the comments made for surge motion also apply here for pitch. The numerical results are well in accordance with the quasi-steady theory, but this only applies for the low-frequencies in the experiment. At high frequency, a large increase in thrust oscillation is once again obtained. In addition, the phase difference has now diverged from the theoretical value. This time, a slight increase in the thrust amplitude is also observed between the two low-frequency cases, but it is not comparable with the significant rise experienced at $f = 5\ Hz$. It should be noted that the larger amplitudes of variations measured for pitch, compared to those obtained for surge, can be explained by the larger reduced velocity ΔV^* considered.

Similarly to surging, the mean thrust obtained numerically during pitching is found to increase minutely with frequency. This time, a similar trend is observed in the experiment.

Table 4: Comparison of rotor thrust for pitch motion with $\Delta V_p^* = 0.072$.

Source	Frequency	$\overline{T}$ [N]	$\lvert\Delta T\rvert$ [N]	$\phi\Delta T$ [deg]
YALES2	$f = 1$ Hz	9.23	0.68	-91.8
	$f = 2$ Hz	9.24	0.68	-91.4
	$f = 5$ Hz	9.24	0.69	-92.5
Exp.	$f = 1$ Hz	9.77	0.80	-94.8
	$f = 2$ Hz	9.73	0.85	-92.1
	$f = 5$ Hz	9.86	1.45	-77.8

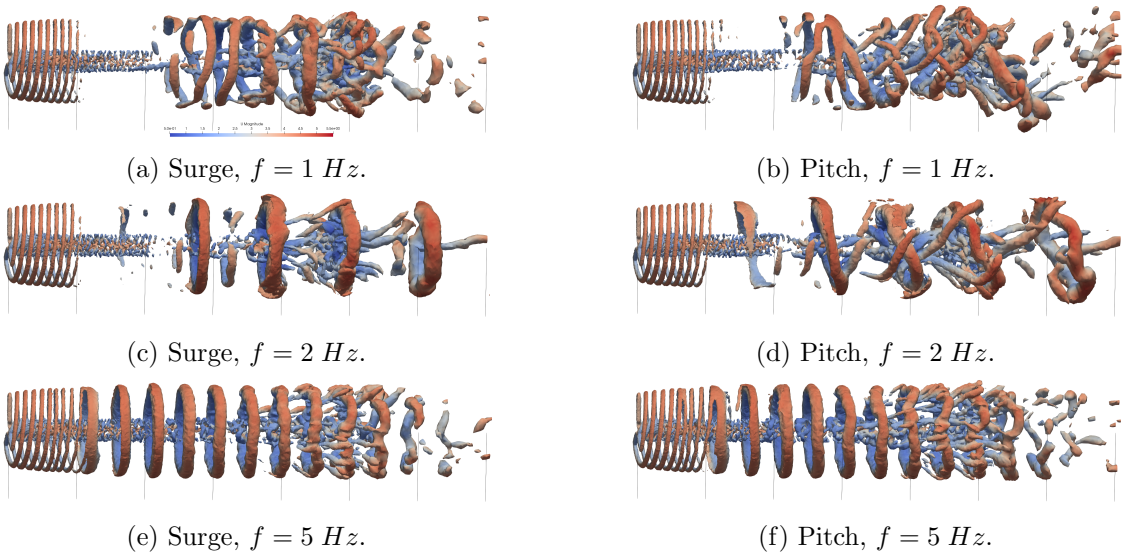

(a) Surge, $f = 1\ Hz$. (b) Pitch, $f = 1\ Hz$.

(c) Surge, $f = 2\ Hz$. (d) Pitch, $f = 2\ Hz$.

(e) Surge, $f = 5\ Hz$. (f) Pitch, $f = 5\ Hz$.

Figure 6: Instantaneous iso-contours of $Q = 20\ s^{-2}$ coloured by the velocity amplitude for the six motion cases at $t = t_f$, vertical lines are placed every $z = 1D$.

6. Wake

In addition to the loads, the numerical simulations permit access to additional information such as the development of the wake. It should be reminded that the domain size and mesh resolution used only allow to draw conclusions on the near and mid-wake, up to approximately $z = 5D$.

Due to the motions, the formation of three-dimensional vortical structures in the mid-wake was observed. In order to visualise them, iso-contours plots of the so-called *Q-criterion* are given in Figure 6. The Q-criterion is widely used in CFD as it permits the formation of envelopes around vortical structures. For wind turbine applications, it is often used to visualise the development of tip vortices. The iso-contours are plotted for $Q = 20\ s^{-2}$ and coloured by the velocity amplitude. They are given for the final time step and lines separated by the distance $z = 1D$ are traced to give a distance indicator.

First, in all figures, one can clearly observe the formation of the typical tip and root vortices in the near-wake. For the pitch and surge cases at $f = 5\ Hz$, one particular thing to note is that the distance between two successive tip vortices sometimes vary due to the motion. This can even cause two vortices to collide as in the high-frequency pitching case (Figure 6f). This phenomenon was already observed for pitch motions in the literature [13], even if, here, it

remains relatively small due to the amplitude and frequency considered.

The main phenomenon to observe in Figure 6 is the formation of vortex rings enveloping the wake for both $f = 2\ Hz$ and $f = 5\ Hz$. These three-dimensional coherent vortical structures are formed for both surge and pitch motions.

It can be checked that these vortex rings are formed at motion frequency. Indeed, let's consider a probe in the $x = 0$ plane, at a vertical position corresponding to the borders of the wake and a streamwise position within the region where these structures appear. This probe sees vortices (the vortex ring footprint in the plane) passing by at a certain frequency. The vertical component of the velocity U_y is expected to oscillate between positive and negative velocities at this frequency. This quantity is plotted in Figure 7 for the surge case at $f = 2Hz$. One can clearly see the periodic oscillation in the vertical velocity corresponding to the passage of the vortex rings at this location. There is no need to show the spectrum to identify clear oscillations at the corresponding motion period $T = 0.5s$. The procedure can be repeated at various streamwise positions with similar observations. Identical conclusions are drawn for the high-frequency case and similarly for pitch motion.

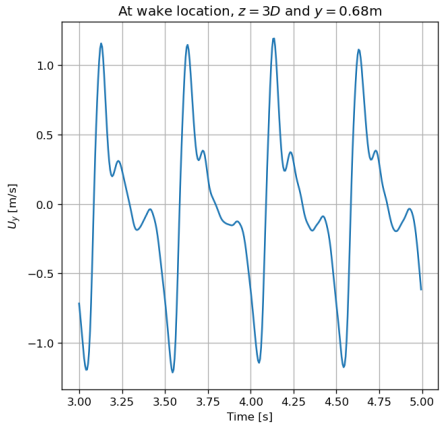

Figure 7: Temporal evolution of the vertical velocity U_y at location $(x = 0; y = 0.68\ m; z = 3D)$, surge case with $f = 2\ Hz$.

When vortex rings are formed, they have similar shape and sizes, with little impact of the frequency or the type of motion considered. Yet, these vortex rings are slightly tilted when pitch motion is imposed. This is particularly true for $f = 2\ Hz$ in which the amplitude of motion is larger than for $f = 5\ Hz$. However, one difference that can be observed, is that the vortex rings are formed earlier in the wake at high frequency. Indeed, for both surging and pitching at $f = 5\ Hz$, these structures appear right after the tip vortices dissipate (about $z = 1D$) while they are fully formed downwind for $f = 2\ Hz$. For the lowest frequency ($f = 1\ Hz$), and again for both surging and pitching, vortex rings cannot be clearly identified. Some vortical structures are formed later in the wake but they do not form rings, and they are not formed at the corresponding motion frequency. In a general manner, the flow is more chaotic at this low frequency.

Concerning the pitch case, some vertical wake meandering can also be noticed at low frequency. Indeed, by looking at the Figure 6b, one can see the wake deflecting downward around $z = 3D$, then upward and finally downward again. Those findings can be completed with those of Duan et al. [14] who also observe the formation of vortex rings during surge motion. They considered higher reduced frequencies than in this study ($f_r = fD/U_\infty = 0.56, 1.11, 2.23$ and $f_r = 0.15, 0.3, 0.6$ respectively) and noted that these coherent structures could not be formed anymore at very high frequency. Concerning the breakdown of these vortex rings, they put forward the hypothesis that it was initiated by the expansion of the central vortices, interacting with the outer structures. Such a phenomenon seems to occur in the figures from about $z = 4D$ with the central vortices losing their coherence and expanding. However, particularly

for $f = 5\ Hz$, the vortex rings also seem to become distorted starting from $z = 4D$, probably due to differences in velocities all around the ring. In addition, the flow downwind of $z = 5D$ should be looked at with caution, as the mesh resolution is quite low in this area. Finally, those results could be completed by including the tower and the nacelle, which would respectively interact with the tip and root vortices, and by considering more realistic wind conditions such as sheared wind that could deform the vortex rings.

7. Conclusions

In this study, an experimental setup developed to analyze the aerodynamics of a scaled wind turbine under prescribed floating motions is reproduced by means of a large-eddy simulation numerical model. The setup consists of a wind turbine scale model mounted on top of a six degrees of freedom hexapod and tested in a wind tunnel. The tests are emulated using the LES code *YALES2* implemented with an actuator line approach. The experiments show that the motion frequency has an effect on the thrust force, regardless of the actuated degree of freedom and motion velocity: for frequencies greater than 4 Hz the thrust force variation induced by the motion increases deviating from a quasi-steady prediction. The numerical simulations show a good agreement with the experimental results only for reduced frequencies below that value, while for greater values they still predict a quasi-steady variation. Finally, the use of LES permitted the acquisition of further information, such as insights on the wake. In particular, characteristic motion frequencies appeared in the wake, especially at the highest frequencies, and wake meandering was also observed under certain pitch conditions.

References

[1] Fontanella A et al. 2021 UNAFLOW: a holistic wind tunnel experiment about the aerodynamic response of floating wind turbines under imposed surge motion *WES* **6(5)** 1169-1190
[2] Johlas H M et al. 2019 Large eddy simulations of floating offshore wind turbine wakes with coupled platform motion. *J. Phys.: Conf. Ser.* **1256**
[3] Li Z, Dong G and Yang X 2022 Onset of wake meandering for a floating offshore wind turbine under side-to-side motion. *Journal of Fluid Mechanics* **934** A29
[4] Fontanella A, Da Pra G, Belloli M 2023 Integrated Design and Experimental Validation of a Fixed-Pitch Rotor for Wind Tunnel Testing. *Energies* **16(5)** 2205
[5] Taruffi F, Novais F, Viré A 2023 An experimental study on the aerodynamic loads of a floating offshore wind turbine under imposed motions *Wind Energy Science Discussions* [preprint]
[6] Moureau V, Domingo P and Vervisch L 2011 Design of a massively parallel CFD code for complex geometries. *Comptes Rendus Mécanique* **339** 141-148
[7] Benard P, Viré A, Moureau V, Lartigue G, Beaudet L, Deglaire P and Bricteux L 2018 Large-Eddy Simulation of wind turbines wakes including geometrical effects. *Computers & Fluids* **173** 133–139
[8] Germano M, Piomelli U, Moin P and Cabot W H 1991 A dynamic subgrid-scale eddy viscosity model. *Physics of Fluids A: Fluid Dynamics* **3** 1760–1765
[9] Lilly D K 1992 A proposed modification of the Germano subgrid-scale closure method. *Physics of Fluids A: Fluid Dynamics* **4** 633–635
[10] Sørensen, J N and Shen W Z 2002 Numerical Modeling of Wind Turbine Wakes. *Journal of Fluids Engineering* **124** 393–399
[11] Cioni S, Papi F, Pagamonci L, Bianchini A, Ramos-García N, Pirrung G, Corniglion R, Lovera A, Galván J, Boisard R, Fontanella A, Schito P, Zasso A, Belloli M, Sanvito A, Persico G, Zhang L, Li Y, Zhou Y, Mancini S, Boorsma K, Amaral R, Viré A, Schulz CW, Netzband S, Soto Valle R, Marten D, Martín-San-Román R, Trubat P, Molins C, Bergua R, Branlard E, Jonkman J, Robertson A 2023 On the characteristics of the wake of a wind turbine undergoing large motions caused by a floating structure: an insight based on experiments and multi-fidelity simulations from the OC6 Phase III Project. *Wind Energy Science Discussions* **2023** 1-37
[12] Pope, S B 2004 Ten questions concerning the large-eddy simulation of turbulent flows. *New Journal of Physics* **6** 35–35
[13] Fang Y, Duan L, Han Z, Zhao Y and Yang H 2020 Numerical analysis of aerodynamic performance of a floating offshore wind turbine under pitch motion. *Energy* **192** 116621
[14] Duan L, Sun Q, He Z and Li G 2022 Wake topology and energy recovery in floating horizontal-axis wind turbines with harmonic surge motion. *Energy* **260** 124907